

Available online at [www.sciencedirect.com](http://www.sciencedirect.com)**ScienceDirect**

ELSEVIER

journal homepage: [www.elsevier.com/locate/he](http://www.elsevier.com/locate/he)

# Controllable transformation of sheet-like CoMo-hydro(oxide) and phosphide arrays on nickel foam as efficient catalysts for alkali water splitting and Zn–H<sub>2</sub>O cell

Puxuan Yan <sup>a,b</sup>, Yanjing Qin <sup>a</sup>, Yuting Yang <sup>a</sup>, Xue Shao <sup>a</sup>,  
Tayirjan Taylor Isimjan <sup>c, \*\*</sup>, Xiulin Yang <sup>a,\*</sup>

<sup>a</sup> Guangxi Key Laboratory of Low Carbon Energy Materials, School of Chemistry and Pharmaceutical Sciences, Guangxi Normal University, Guilin, 541004, China

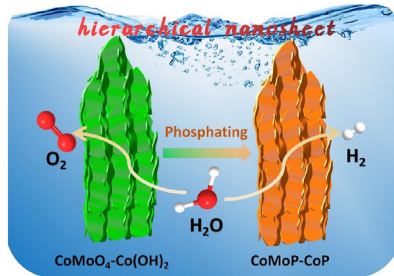
<sup>b</sup> Guangxi Key Laboratory of Information Materials, School of Material Science and Engineering, Guilin University of Electronic Technology, Guilin 541004, China

<sup>c</sup> Saudi Arabia Basic Industries Corporation (SABIC) at King Abdullah University of Science and Technology (KAUST), Thuwal 23955-6900, Saudi Arabia

## HIGHLIGHTS

- CoMoO<sub>4</sub>–Co(OH)<sub>2</sub> and CoMoP–CoP nanosheets on nickel foam are precisely fabricated by a controllable method.
- Both catalysts exhibited high electrocatalytic activity and stability for OER and HER, respectively.
- The two catalysts constructed overall water splitting system shows robust activity and stability.
- The unique structure and strong electronic interactions between the different components lead to excellent performance.

## GRAPHICAL ABSTRACT



## ARTICLE INFO

### Article history:

Received 30 November 2021

Received in revised form

4 April 2022

Accepted 15 May 2022

Available online 8 June 2022

## ABSTRACT

Design and synthesis of cost-effective electrocatalysts with remarkable activity and stability is highly desirable for renewable energy devices. Herein, we have successfully constructed sheet-like CoMoO<sub>4</sub>–Co(OH)<sub>2</sub> and CoMoP–CoP arrays on nickel foam (NF) through chemical etching ZIF-67 arrays and phosphorization in sequence. Series CoMoO<sub>4</sub>–Co(OH)<sub>2</sub>/NF as anode and CoMoP–CoP/NF as cathode showed excellent electrocatalytic activity and stability in alkali water splitting, where the combined catalysts only need 1.67 V cell voltage

\* Corresponding author.

\*\* Corresponding author.

E-mail addresses: [isimjant@sabic.com](mailto:isimjant@sabic.com) (T.T. Isimjan), [xlyang@gxnu.edu.cn](mailto:xlyang@gxnu.edu.cn) (X. Yang).

<https://doi.org/10.1016/j.ijhydene.2022.05.136>

0360-3199/© 2022 Hydrogen Energy Publications LLC. Published by Elsevier Ltd. All rights reserved.

**Keywords:**

Sheet-like arrays  
 $\text{CoMoO}_4\text{--Co(OH)}_2(\text{P})$   
 Synergistic effect  
 Water splitting  
 $\text{Zn}\text{--H}_2\text{O}$  cell

to drive  $10 \text{ mA cm}^{-2}$  and obtain robust high current stability at  $500 \text{ mA cm}^{-2}$  for 110 h with almost no attenuation. In addition, using  $\text{CoMoP--CoP/NF}$  as the cathode of a  $\text{Zn--H}_2\text{O}$  cell can provide a power density of  $11.5 \text{ mW cm}^{-2}$  and a stable 170 h for simultaneous  $\text{H}_2$  and electricity generation. The excellent performance of the system is attributed to the unique sheet-like array morphology of combined catalysts providing large surface area and rich pore structure conducive to electrolyte diffusion and gas emission, as well as the synergies between the different components providing more catalytic active sites.

© 2022 Hydrogen Energy Publications LLC. Published by Elsevier Ltd. All rights reserved.

## Introduction

In view of the serious carbon dioxide pollution caused by the excessive consumption of traditional fossil fuels, considerable efforts have been devoted to find clean and sustainable energy sources [1]. Hydrogen is deemed as an ideal sustainable chemical energy carrier, owing to its high energy density [2]. Electrochemical water splitting is generally regarded as prospective technologies for industrial-scale hydrogen production. Currently,  $\text{Pt/C}$  and  $\text{RuO}_2$  noble catalysts have been considered as pioneering electrocatalytic hydrogen evolution reaction (HER) and oxygen evolution reaction (OER) catalysts [3,4], but their expensiveness and scarcity limit the industrial applications [5], prompting us to investigate non-noble metal catalysts. However, non-precious metal catalysts still require higher overpotential compared to precious metal-based catalysts, which unfortunately impedes large-scale hydrogen generation. Therefore, the development of low-cost and efficient transition metal-based catalysts is necessary for hydrogen production.

The state-of-the-art transition metals OER catalysts reported in the literature are based on Ni active sites that raise a severe environmental concern (Table S1) [6]. Cobalt hydroxide as an alternative is a reasonable OER electrocatalyst, which can serve as an alternative to  $\text{RuO}_2$  due to its low cost and less environmental impact. However, its insufficient active surface and high charge transfer resistance can't significantly improve sluggish OER kinetics [7,8]. Based on this, doping with other transition metal compounds is an effective strategy for improving catalytic performance through a synergistic effect. Chen et al. [9] reported a hybrid composite of  $\text{CoO}_x\text{--CoMoO}_4$  nanorod, which shows excellent OER performance due to the electron transfer between two components. Wang et al. [10] exhibited the hierarchical heterostructure  $\text{CoP}_3\text{--NiMoO}_4$  nanosheets for overall water splitting on Ni foam. The HER performance originates from electronegativity of P atoms to capture positively charged protons [11]. Meanwhile, to meet the industrial requirements, the catalyst still faces severe challenges to continuously, rapidly and stably generate  $\text{O}_2$  and  $\text{H}_2$  at high current density ( $\geq 500 \text{ mA cm}^{-2}$ ) [12]. So the electrocatalysts required for overall water splitting still need to be further optimized through design strategies. The HER catalyst can serve as the cathode for  $\text{Zn--H}_2\text{O}$  cells that simultaneously generate electricity and hydrogen to reduce further the additional electricity required for overall water splitting [13]. While, the robust stability and mechanism of  $\text{Zn--H}_2\text{O}$  cell still need to be explored based on transition metal phosphides.

Herein, we reported a novel multifunctional  $\text{CoMoO}_4\text{--Co(OH)}_2/\text{NF}$  and  $\text{CoMoP--CoP/NF}$  combined catalysts that can be used for OER, HER, alkali water splitting and  $\text{Zn--H}_2\text{O}$  cell. The synthesis process of two hybrids is as follows, where the sheet-like ZIF-67 arrays were firstly synthesized on the surface of NF via dipping method. Then, the unstable ZIF-67 arrays in water were transformed into hierarchical  $\text{CoMoO}_4\text{--Co(OH)}_2$  nanosheets by immersion etching method. Finally, it was further phosphated into  $\text{CoMoP--CoP}$  nanosheets. The microstructure, crystal structure, specific surface area, chemical state and composition of the  $\text{CoMoO}_4\text{--Co(OH)}_2/\text{NF}$  and  $\text{CoMoP--CoP/NF}$  hybrids have been systematically studied. Subsequently, we designed a system including “ $\text{CoMoO}_4\text{--Co(OH)}_2/\text{NF}$  had high OER activity, and  $\text{CoMoP--CoP/NF}$  showed better HER activity”, and then their combination was used as high current alkali water splitting. Besides, the  $\text{CoMoP--CoP/NF}$  was also adopted as the cathode of alkaline  $\text{Zn--H}_2\text{O}$  cell, which could release  $\text{H}_2$  and generate electricity at the same time. Most importantly, the optimized catalysts showed low overpotential and good stability at high current density ( $500 \text{ mA cm}^{-2}$ ), which is essential for industrial applications. In short, this work proposes a facile catalyst synthesis strategy that can be applied to both  $\text{Zn--H}_2\text{O}$  cell and alkali water splitting.

## Experimental section

### $\text{CoMoO}_4\text{--Co(OH)}_2/\text{NF}$ and $\text{Co(OH)}_2/\text{NF}$

ZIF-67/NF was fabricated by our reported work (detailed in supporting information) [14]. Then,  $\text{Na}_2\text{MoO}_4$  (300 mg) was dissolved in 20 mL deionized water, and heated up to  $80^\circ\text{C}$ . After that, ZIF-67/NF was fixed in the  $\text{Na}_2\text{MoO}_4$  solution, gently stirred for 1 h. The resulted light blue sample was washed with deionized water, and dried at  $60^\circ\text{C}$ , which was nominated as  $\text{CoMoO}_4\text{--Co(OH)}_2/\text{NF}$ . As a comparison, ZIF-67/NF was set in the deionized water, and stirred for 12 h. The light blue sample was rinsed and dried in the same conditions, and was designated as  $\text{Co(OH)}_2/\text{NF}$ . Moreover,  $\text{RuO}_2/\text{NF}$  was assembled by the reported method [14], the loading of  $\text{RuO}_2$  was set to  $2.0 \text{ mg cm}^{-2}$  (detailed in supporting information).

### $\text{CoMoP--CoP/NF}$ and $\text{CoP/NF}$

$\text{CoMoO}_4\text{--Co(OH)}_2/\text{NF}$  and  $\text{Co(OH)}_2/\text{NF}$  were converted into  $\text{CoMoP--CoP/NF}$  and  $\text{CoP/NF}$  by gas phosphatization according

to the following method:  $\text{NaH}_2\text{PO}_2$  (0.7 g) was located at the intake side of the tube furnace, then  $\text{CoMoO}_4\text{--Co(OH)}_2/\text{NF}$  was located next to  $\text{NaH}_2\text{PO}_2$  in direction of airflow. Then the temperature was rose from room temperature to 350 °C at 5 °C min<sup>-1</sup>, and maintained for 3 h under Ar atmosphere. The resulted black sample was nominated as  $\text{CoMoP}\text{--CoP/NF}$ . As a comparison,  $\text{CoP}/\text{NF}$  was also prepared with  $\text{Co(OH)}_2/\text{NF}$  by the same phosphatization. Furthermore,  $\text{Pt/C}/\text{NF}$  was installed in the same method as  $\text{RuO}_2/\text{NF}$ , the loading of Pt/C were set to 1.0 mg cm<sup>-2</sup>.

### Electrochemical measurement

The electrocatalytic activity for OER and HER was estimated by the standard three-electrode mode of electrochemical workstation (Biologic VMP3) with 1.0 M KOH. The pH value of the 1.0 M KOH freshly prepared was 13.5 by pH meter and RHE voltage calibration in Fig. S1. The reference electrode and the counter electrode were saturated calomel electrode and carbon plate, respectively. The details were discussed in the supporting information (experimental section). For alkali water splitting, the performances were evaluated by two-electrode mode in 1.0 M KOH solution. The designed  $\text{CoMoO}_4\text{--Co(OH)}_2/\text{NF}^{(+)}$  and  $\text{CoMoP}\text{--CoP/NF}^{(-)}$  catalyst acted as anode and cathode electrodes, respectively. Then, we continued to evaluate the catalysts in 30 wt% KOH solution that simulated industrial application conditions. We particularly explored the electrocatalytic activity and stability of the catalysts under high current density conditions. Aimed at alkaline Zn–H<sub>2</sub>O cell, it was carried out in the mixture of 6.0 M KOH with 0.2 M  $\text{Zn}(\text{AC})_2$ . Zn plate and  $\text{CoMoP}\text{--CoP/NF}$  were used as anode and cathode, respectively. The power density was calculated by the polarization curves, which performed by LSV method at 10 mV s<sup>-1</sup>. The long-time durability was measured at 10 mA cm<sup>-2</sup> using LAND testing system.

## Results and discussion

### In-situ conversion strategy and crystallinity analysis

The  $\text{CoMoO}_4\text{--Co(OH)}_2/\text{NF}$  and  $\text{CoMoP}\text{--CoP/NF}$  were finely designed through ZIF-67 in-situ conversion and phosphatizing procedure in Fig. 1a. Sheet-like ZIF-67 is evenly self-assembled on the surface of NF by dipping process [14]. Fig. S2 shows the characteristic peaks of ZIF-67 crystal that match previously published ZIF-67 [15,16]. ZIFs crystal is synthesized via the coordination of metal ions and imidazolate ligands [17]. Previous reports demonstrate that ZIF-67 is unstable in water and etched into released  $\text{Co}^{2+}$  ions [18]. ZIF-67 could be transformed into light blue  $\text{CoMoO}_4\text{--Co(OH)}_2$  via dipping in  $\text{NaMoO}_4$  water solution (Fig. S3a), and the quantitative ratio between  $\text{Co(OH)}_2$  and  $\text{CoMoO}_4$  was calculated as 3.4:1 (Table S2). Then,  $\text{CoMoO}_4\text{--Co(OH)}_2$  was converted into black  $\text{CoMoP}\text{--CoP}$  during phosphatizing. The loadings of  $\text{CoMoO}_4\text{--Co(OH)}_2$  and  $\text{CoMoP}\text{--CoP}$  were respectively 6.9 and 7.3 mg cm<sup>-2</sup>.

Fig. 1a and b illustrate the X-ray powder diffraction (XRD) patterns of  $\text{CoMoO}_4\text{--Co(OH)}_2$  and  $\text{CoMoP}\text{--CoP}$ , together with  $\text{Co(OH)}_2$  and  $\text{CoP}$  as comparative catalysts. The diffraction peaks at 11.5°, 23.2°, 34.5° and 59.8° can be indexed to the (003), (006), (102) and (110) planes of hexagonal  $\text{Co(OH)}_2$  (JCPDS: 46-0605), respectively. The diffraction peaks at 23.3°, 27.5°, 32.9°, 36.8° and 48.8° can be corresponding to the (021), (-202), (-222), (400) and (-133) planes of monoclinic  $\text{CoMoO}_4$  (JCPDS: 21-0868), respectively. This result explains that partial cobalt ions dissociated from ZIF-67 react with molybdate ions according to  $\text{MoO}_4^{2-} + \text{Co}^{2+} = \text{CoMoO}_4 \downarrow$ , another part react with hydroxide ions to generate cobalt hydroxide according to the  $2\text{OH}^- + \text{Co}^{2+} = \text{Co(OH)}_2 \downarrow$ , because the sodium molybdate solution is weak alkaline. XRD patterns of comparative

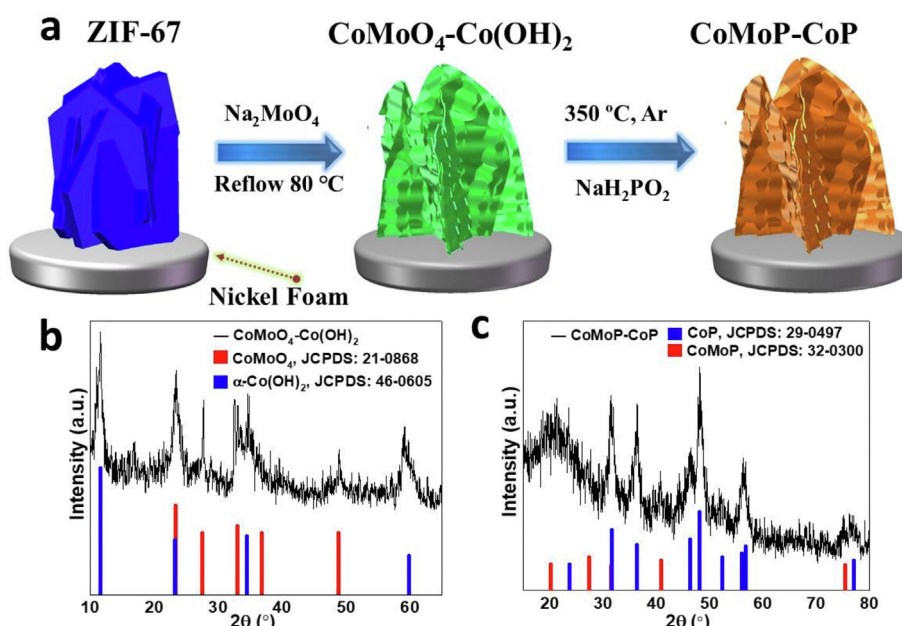


**Fig. 1 – (a)** The fabricating scheme of  $\text{CoMoO}_4\text{--Co(OH)}_2/\text{NF}$  and  $\text{CoMoP}\text{--CoP/NF}$ . XRD patterns of (b)  $\text{CoMoO}_4\text{--Co(OH)}_2$  and (c)  $\text{CoMoP}\text{--CoP}$ .

$\text{Co(OH)}_2$  and CoP are the same as that of the corresponding substance in the  $\text{CoMoO}_4\text{--Co(OH)}_2$  and  $\text{CoMoP}\text{--CoP}$  (Figs. S4a–b), implying that ZIF-67 in water is converted to  $\text{Co(OH)}_2$ , and then convert into CoP after phosphating.

### Microstructure analysis

The hierarchical and array structure of two catalysts was characterized by scanning electron microscopy (SEM). As shown in Fig. 2a, ZIF-67 is a smooth sheet with a thickness of ~154 nm. After ZIF-67 was transformed into  $\text{CoMoO}_4\text{--Co(OH)}_2$ , its smooth sheets convert into hierarchical sheets composed of many nanosheets (Fig. 2b). The  $\text{CoMoP}\text{--CoP}$  structure has little change during phosphating compared to  $\text{CoMoO}_4\text{--Co(OH)}_2$  (Fig. 2c). Moreover, according to  $\text{N}_2$  adsorption-desorption isotherm (Fig. 2d), they belong to typical type-III isotherm with the hysteresis loop. The specific surface area of  $\text{CoMoP}\text{--CoP}$  is  $25.5 \text{ m}^2 \text{ g}^{-1}$ , it is lower than  $\text{CoMoO}_4\text{--Co(OH)}_2$  ( $51.6 \text{ m}^2 \text{ g}^{-1}$ ). The average gap sizes between the interwoven nanosheets of  $\text{CoMoO}_4\text{--Co(OH)}_2$  and  $\text{CoMoP}\text{--CoP}$  are 25.5 and 23.6 nm, respectively, demonstrating a typical mesoporous material, which is beneficial to enhance gas emission and ion diffusion rate [19].

The TEM images reveal that  $\text{CoMoO}_4\text{--Co(OH)}_2$  is composed by nanosheets (Fig. 3a), its 0.767 nm lattice spacing matches the (003) crystal plane of  $\alpha\text{-Co(OH)}_2$  (Fig. 3b). The SAED shows concentric diffraction rings consisting of discrete spots, which can be unambiguously assigned to the (110) plane of  $\alpha\text{-Co(OH)}_2$  and (−222) plane of  $\text{CoMoO}_4$  (Fig. 3c). The high-angle annular

dark field (HAADF) TEM elemental mappings in Fig. 3d demonstrate a uniform distribution of Co, Mo and O in  $\text{CoMoO}_4\text{--Co(OH)}_2$  hybrid.

### XPS analysis

The XPS survey spectra of  $\text{CoMoO}_4\text{--Co(OH)}_2$  and  $\text{CoMoP}\text{--CoP}$  display the co-existence of Co, Mo, O, P and C elements (Fig. S5a). As a calibration standard, we deconvolute the high resolution C 1s region into C=C (284.0 eV), C-C (284.8 eV) and C–N/C–O (286.0 eV) (Fig. S5b) [20]. In Fig. 4a, the Co 2p<sub>3/2</sub> spectrum of  $\text{Co(OH)}_2\text{--CoMoO}_4$  displays two fitting peaks at 780.2 and 781.5 eV, belonging to  $\text{Co}^{2+}$  [2,21], the Co 2p<sub>3/2</sub> region for  $\text{CoMoP}\text{--CoP}$  shows two fitting peaks at 778.3 and 781.2 eV, they respectively match the cobalt phosphide and partial oxide [22,23]. As shown in Fig. 4b, the Mo 3d spectrum of  $\text{CoMoO}_4$  respectively shows the spin orbit doublet Mo 3d<sub>5/2</sub> (231.5 eV) and Mo 3d<sub>3/2</sub> (234.7 eV) [24], the distance between the two peaks is 3.2 eV, this is the feature of the  $\text{Mo}^{6+}$  oxidation state [25]. The two peaks at 227.3 and 230.4 eV of Mo 3d are assigned to  $\text{Mo}^{\delta+}$  species ( $0 < \delta < 4$ ), other two doublets located at 234.9/231.8 eV and 233.1/230.0 eV are assigned to  $\text{Mo}^{6+}$  and  $\text{Mo}^{4+}$ , respectively, indicating the surface oxidation of  $\text{CoMoP}$  [26,27]. In the O 1s region of  $\text{CoMoO}_4\text{--Co(OH)}_2$  (Fig. 4c), three binding energies of 530.0, 531.0 and 532.4 eV respectively correspond to the lattice oxygen, oxygen vacancies and absorbed oxygen species in the metal compounds [14,28]. According to Fig. 4d, in the P 2p region of  $\text{CoMoP}\text{--CoP}$ , the peak at 134.4 eV denotes the P–O binding energy because the phosphide surface is oxidized

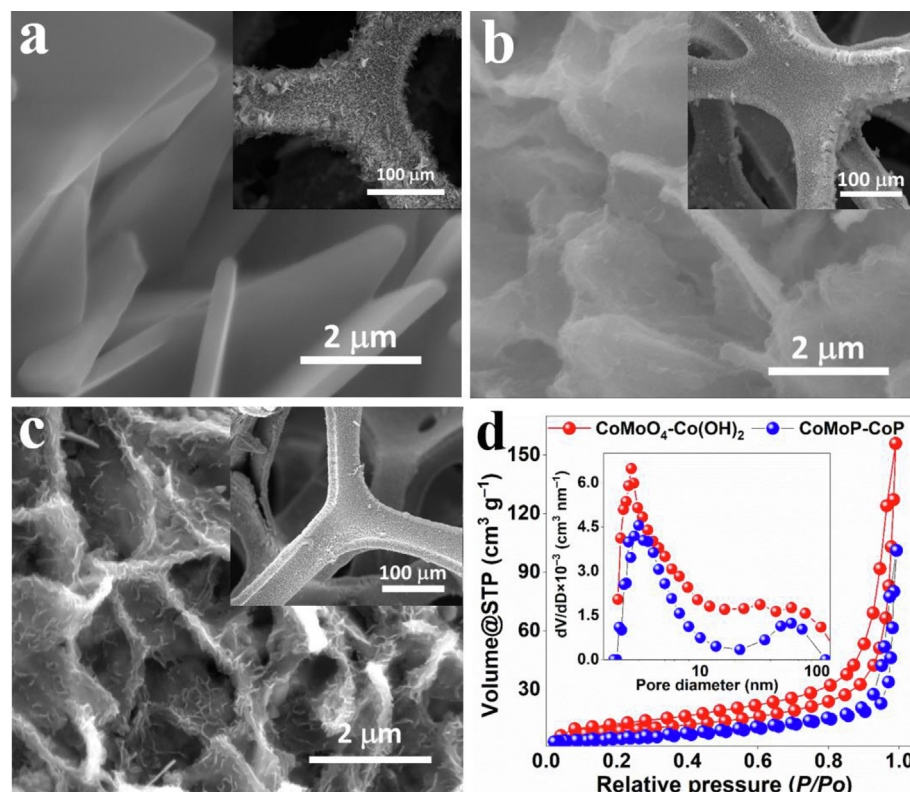


**Fig. 2 – SEM images of (a) ZIF-67/NF, (b)  $\text{CoMoO}_4\text{--Co(OH)}_2/\text{NF}$  and (c)  $\text{CoMoP}\text{--CoP}/\text{NF}$  with different magnifications. (d) Nitrogen adsorption-desorption isotherms of  $\text{CoMoO}_4\text{--Co(OH)}_2$  and  $\text{CoMoP}\text{--CoP}$ .**

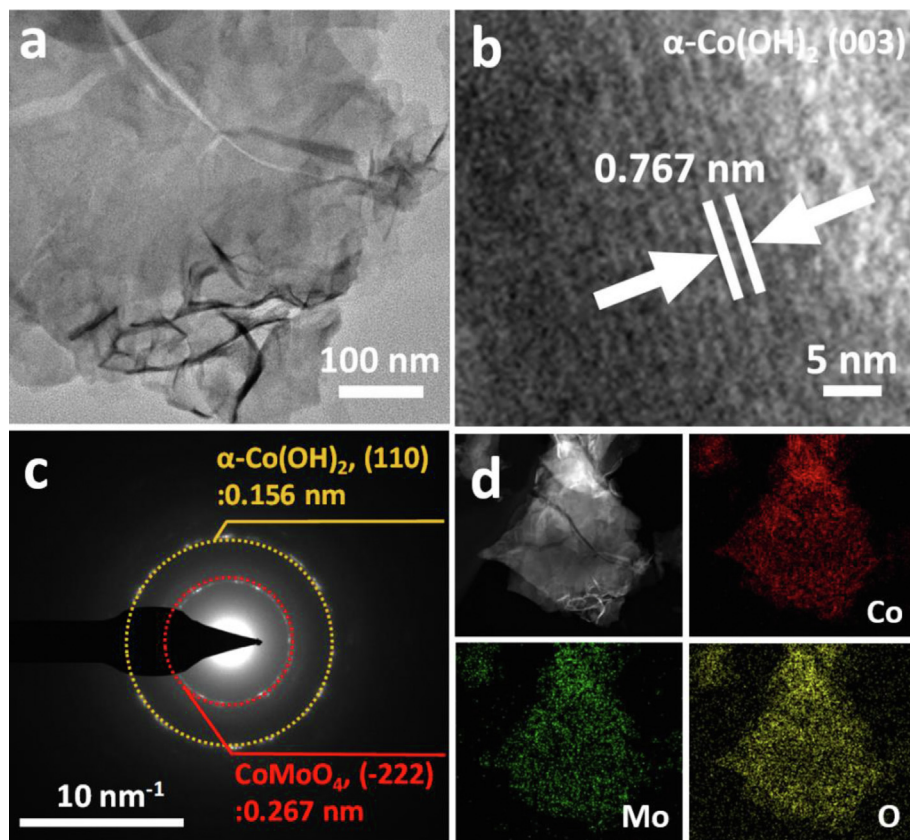


**Fig. 3 – (a, b)** TEM images of  $\text{CoMoO}_4\text{--Co(OH)}_2$ . **(c)** The corresponding selected area electron diffraction (SAED) images of  $\text{CoMoO}_4\text{--Co(OH)}_2$ . **(d)** Elemental mapping images of Co, Mo and O of  $\text{CoMoO}_4\text{--Co(OH)}_2$ .

[4], two fitting peaks at 130.0 ( $\text{P } 2p_{3/2}$ ) and 130.9 eV ( $\text{P } 2p_{1/2}$ ) are the binding energy of metal-P [29]. Notably, the Co  $2p_{3/2}$  of  $\text{CoMoO}_4\text{--Co(OH)}_2$  and CoMoP–CoP produces a negative shift of 0.42 and 0.24 eV relative to  $\text{Co(OH)}_2$  and CoP, respectively (Figs. S6a–b), indicating the existence of strong electronic interactions between two components of two catalysts [30], which in turn facilitates charge transfer, thereby enhancing OER and HER performance [9,31].

#### OER and HER analysis

The OER performance of different catalysts are initially analyzed in alkaline media. According to Fig. 5a, the  $\text{CoMoO}_4\text{--Co(OH)}_2/\text{NF}$  presents a lower overpotential of 245.5 mV at  $10 \text{ mA cm}^{-2}$ , and outperforms those of  $\text{RuO}_2/\text{NF}$  (253.6 mV),  $\text{CoMoP--CoP/NF}$  (317.8 mV), and  $\text{Co(OH)}_2/\text{NF}$  (292.7 mV), respectively. Besides, the catalyst also exceeds most of the high-performance OER catalysts reported in the literature (Table S1) [9,10,32–45]. Since ZIF-67/NF cannot be converted to  $\text{CoMoO}_4/\text{NF}$  in situ, we reference the literature for array-type  $\text{CoMoO}_4$  (JCPDS: 21-0868) catalysts supported on nickel foam or carbon cloth, and the overpotentials were between 302 and 350 mV in Table S3. Particularly, the performance advantage is more prominent at higher current densities. The results imply a observable synergistic effect between Co and Mo species, namely the octahedral coordinated  $\text{Co}^{2+}$  in the  $\text{CoMoO}_4$  is easier to oxidize to  $\text{Co}^{3+}$  in  $\text{CoOOH}$ , this evidently reinforces the electrochemical activity [42]. The  $\text{CoMoO}_4\text{--Co(OH)}_2/\text{NF}$  has the

Tafel slope of  $55.5 \text{ mV dec}^{-1}$ , it is smaller than those of  $\text{Co(OH)}_2/\text{NF}$  ( $71.9 \text{ mV dec}^{-1}$ ) and  $\text{RuO}_2/\text{NF}$  ( $59.6 \text{ mV dec}^{-1}$ ) (Fig. 5b). In Fig. 5c, compared to the literatures of similar catalysts,  $\text{CoMoO}_4\text{--Co(OH)}_2/\text{NF}$  processes the lower values of the Tafel slope and overpotential, which indicate better catalytic kinetics of OER [46]. Many studies have found that the ECSA grows with the increasing electrochemical double layer capacitance ( $C_{dl}$ ) [47]. In Fig. 5d and Fig. S7, the  $C_{dl}$  of  $\text{CoMoO}_4\text{--Co(OH)}_2/\text{NF}$  is  $374.2 \text{ mF cm}^{-2}$ , higher than those of  $\text{Co(OH)}_2/\text{NF}$  and  $\text{RuO}_2/\text{NF}$ , indicating its larger electrochemically active surface area [47]. The Nyquist plots are acquired by electrochemical impedance spectroscopy (EIS) [48]. As shown in Fig. S8a, the smaller semicircle diameter, the faster the charge transport rate of the electrode [49],  $\text{CoMoO}_4\text{--Co(OH)}_2/\text{NF}$  exhibits smaller semicircular diameter compared to  $\text{Co(OH)}_2/\text{NF}$ , implying that it has faster charge transfer ability. Furthermore,  $\text{CoMoO}_4\text{--Co(OH)}_2/\text{NF}$  can achieve a  $0.01 \text{ s}^{-1}$  turnover frequency (TOF) value at 313.3 mV overpotential (Fig. S9, Table S2), it is much lower than the 374.8 mV overpotential of  $\text{Co(OH)}_2/\text{NF}$ , revealing a better intrinsic activity of  $\text{CoMoO}_4\text{--Co(OH)}_2/\text{NF}$  [50].

The HER properties of different catalysts were evaluated via LSV in the three-electrode mode. The CoMoP–CoP/NF shows a lower 123.9 mV overpotential at  $10 \text{ mA cm}^{-2}$  in  $1.0 \text{ M KOH}$ , in comparison with CoP/NF (219.3 mV) and  $\text{CoMoO}_4\text{--Co(OH)}_2/\text{NF}$  (237.1 mV) (Fig. S10a). According to Fig. S10b, CoMoP–CoP/NF has the Tafel slope of  $62.5 \text{ mV dec}^{-1}$ , it is less than those of CoP/NF ( $114.6 \text{ mV dec}^{-1}$ ) and  $\text{CoMoO}_4\text{--Co(OH)}_2/\text{NF}$  ( $196.9 \text{ mV dec}^{-1}$ ), this result reveals that the HER of

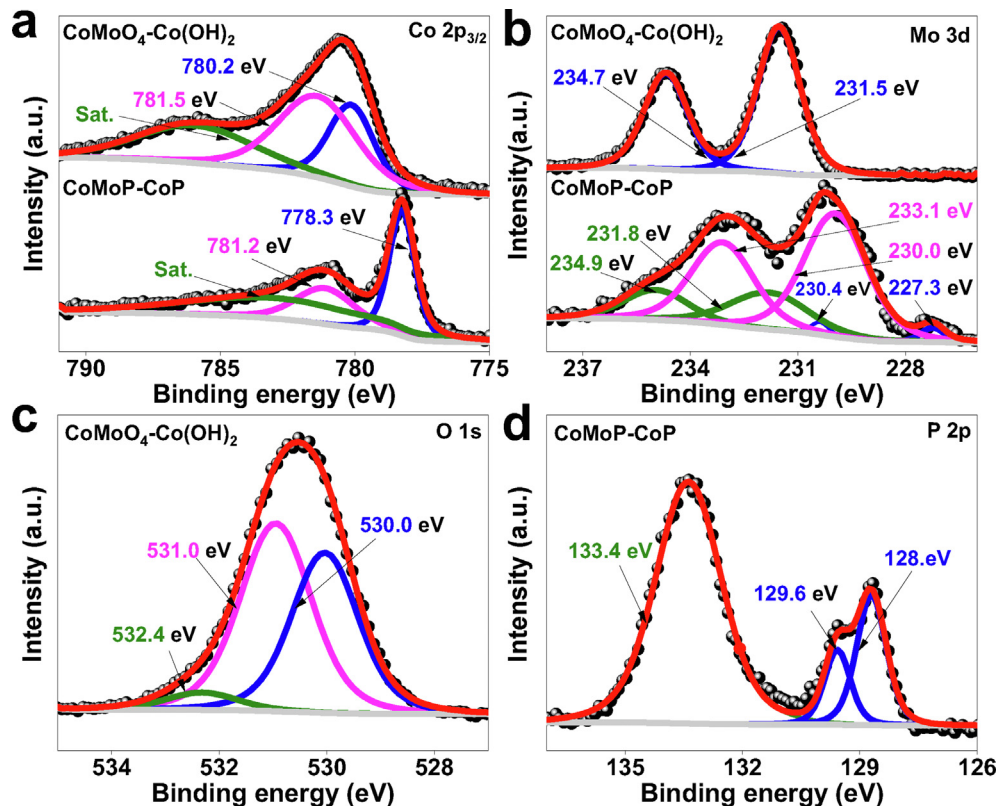


Fig. 4 – The XPS of (a) Co 2p<sub>3/2</sub>, (b) Mo 3d for CoMoP–CoP and CoMoO<sub>4</sub>–Co(OH)<sub>2</sub>, (c) O 1s for CoMoO<sub>4</sub>–Co(OH)<sub>2</sub>, (d) P 2p for CoMoP–CoP.

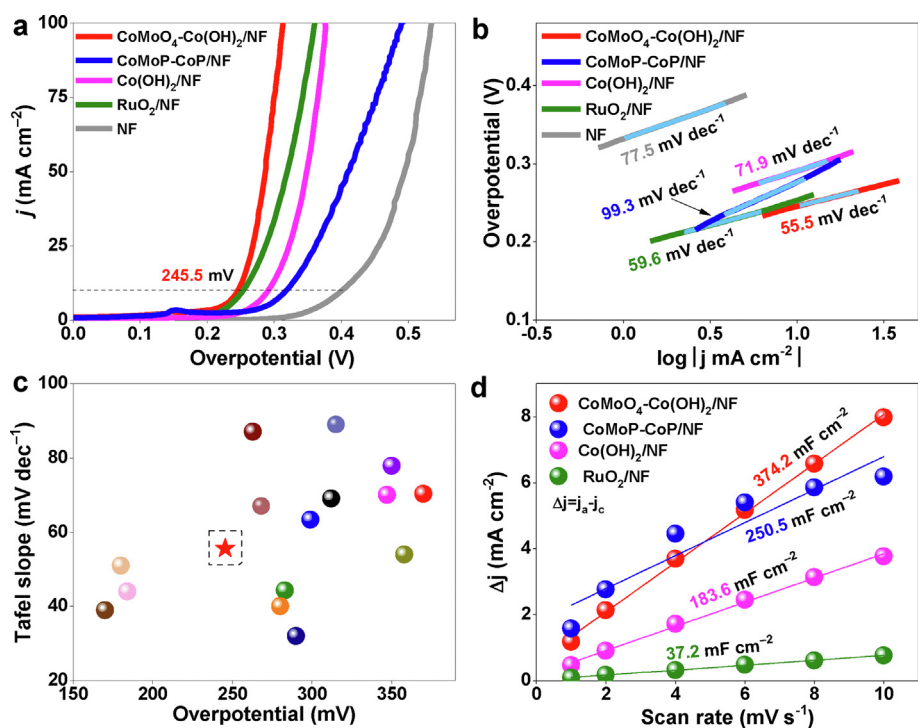


Fig. 5 – (a) Polarization curves of NF, RuO<sub>2</sub>/NF, Co(OH)<sub>2</sub>/NF, CoMoP–CoP/NF and CoMoO<sub>4</sub>–Co(OH)<sub>2</sub>/NF. (b) Tafel slope of corresponding OER. (c) Comparison of OER performance between CoMoO<sub>4</sub>–Co(OH)<sub>2</sub>/NF and similar published catalysts (Table S1). (d) C<sub>dl</sub> diagram summarized by the CV curves of different voltage scan rates.

CoMoP–CoP/NF may follow by Volmer–Heyrovsky pathway [51], which suggests that electrochemical desorption is the rate determining step [52]. As we expected, the optimized CoMoO<sub>4</sub>–Co(OH)<sub>2</sub>/NF was designed as an OER catalyst, which showed a relatively low HER activity reflecting as high overpotential and Tafel slope. CoMoP–CoP/NF exhibits smaller semicircular diameters than that of CoP/NF, showing it has faster charge transfer ability (Fig. S8b). For CoMoO<sub>4</sub>–Co(OH)<sub>2</sub>/NF and CoMoP–CoP/NF catalyst, average relative deviations of voltage are below or equal to 2.0% at 10 mA cm<sup>-2</sup> during 48 h (Figs. S10c–d). Although two catalysts are partially agglomerated after the 48 h stability test, they still showed a complete hierarchical array structure (Fig. S11), demonstrating that they have excellent stability due to the stable and interconnected array structure. Subsequently, the XPS technique was used to probe the changes in the surface chemical states after catalytic stability. The new peak detected at 779.4 eV corresponds to Co<sup>3+</sup> of the CoOOH, which is the surface-active species generated during OER (Fig. S12a) [53,54], while the Mo signal of CoMoO<sub>4</sub> remains unchanged (Fig. S12b). On the other hand, the CoMoP–CoP/NF still retains the original elemental composition and the chemical states due to the electron-rich reduction environment during the HER in Figs. S12c–e [13,55].

#### Alkali water splitting and Zn–H<sub>2</sub>O cell

Based on alkali water splitting, two-electrode mode of CoMoO<sub>4</sub>–Co(OH)<sub>2</sub>/NF<sup>(+)</sup> and CoMoP–CoP/NF<sup>(−)</sup> was constructed. The total voltage required for CoMoO<sub>4</sub>–Co(OH)<sub>2</sub>/NF<sup>(+)</sup>||CoMoP–CoP/NF<sup>(−)</sup> is 1.67 V at 10 mA cm<sup>-2</sup> in 1.0 M KOH (Fig. S13a), it is better than most reported similar catalysts (Fig. S13b). Note that the oxidation peaks between 1.05 and 1.35 V are the contribution of the Co<sup>2+</sup> to Co<sup>3+</sup> conversion on the catalyst surface [56]. Aimed at industrial applications, alkali water splitting is mostly carried out under 30 wt% KOH solution and high current density ( $\geq$ 500 mA cm<sup>-2</sup>) [57]. The voltage of CoMoO<sub>4</sub>–Co(OH)<sub>2</sub>/NF<sup>(+)</sup>||CoMoP–CoP/NF<sup>(−)</sup> is 1.81 V at 500 mA cm<sup>-2</sup> (Fig. 6a), it is close to noble metal catalysts of RuO<sub>2</sub><sup>(+)</sup>||NiS<sub>x</sub>–MoO<sub>3</sub><sup>(−)</sup> and RuO<sub>2</sub><sup>(+)</sup>||Pt/C<sup>(−)</sup> under similar reaction conditions as we previously reported [58]. In addition, we conducted stability tests at 10 and 500 mA cm<sup>-2</sup>, respectively. Even at 500 mA cm<sup>-2</sup> for 110 h of continuous operation, the

average relative deviation of the voltage was still less than 1.7% (Fig. 6b).

The CoMoP–CoP/NF and commercial zinc plate are used as the cathode and anode of the Zn–H<sub>2</sub>O cell, respectively, which can simultaneously produce hydrogen and electricity (Fig. 7a). The power density of the cell is 11.5 mW cm<sup>-2</sup> in the mixture of 6.0 M KOH and 0.2 M Zn(AC)<sub>2</sub> (Fig. 7b), which is higher than CoP/NF (10.1 mW cm<sup>-2</sup>) and most of the reported results in Table S4. In order to observe hydrogen generation on the cathode surface, we assemble a two-electrode system, and many hydrogen bubbles are generated on the surface of CoMoP–CoP/NF (Fig. 7c). As shown in Fig. 7d, an LED light can be lit by two Zn–H<sub>2</sub>O cell with a total voltage of 1.66 V (Fig. S14a) which can drive the alkali water splitting (Fig. S15). In Fig. 7e and Figs. S14b–c, zinc is transformed into hexagonal ZnO (JCPDS: 36-1451) and orthorhombic Zn(OH)<sub>2</sub> (JCPDS: 38-0385) during each 36-h discharge, which are dissolved in the electrolyte and covered on the catalyst to stop the Zn–H<sub>2</sub>O cell. Then we replace the electrolyte, zinc plate, and clean CoMoP–CoP/NF with 0.5 M H<sub>2</sub>SO<sub>4</sub>, the cell is resurrected. So its Zn–H<sub>2</sub>O cell exhibits strong discharge stabilization for more than 170 h by five resurrection operations according to chronopotentiometry curves, indicating that the CoMoP–CoP/NF electrode shows potential reusable value due to its acid resistance. The average relative deviation of its discharge voltage is only 4.9%, showing remarkable discharge stability.

Based on the above discussion, the excellent catalytic activities of CoMoO<sub>4</sub>–Co(OH)<sub>2</sub>/NF and CoMoP–CoP/NF are attributed to the following aspects: (I) Both catalysts show the hierarchical nanosheet structure with high specific surface area, exposing more active sites. Moreover, the array structures benefit gas diffusion and electrolyte transport during electrocatalysis. (II) Both self-supporting catalysts exhibit low charge transfer resistance, enabling lower required potential during electrocatalysis. (III) There are strong electronic interactions between the respective different components of the two catalysts by XPS analysis, this feature promotes the charge transfer and synergistically improves the HER and OER performance. (IV) After electrocatalytic stability, CoMoP–CoP still retains the original chemical structure for HER, while the CoOOH is formed on the surface of CoMoO<sub>4</sub>–Co(OH)<sub>2</sub> as active site for OER [54].

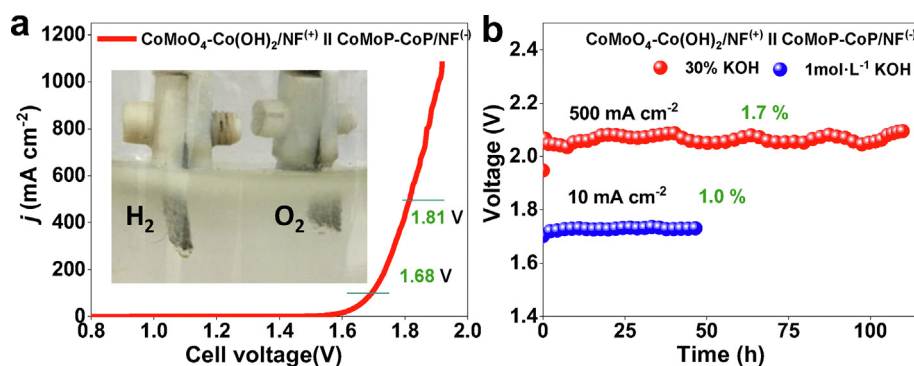
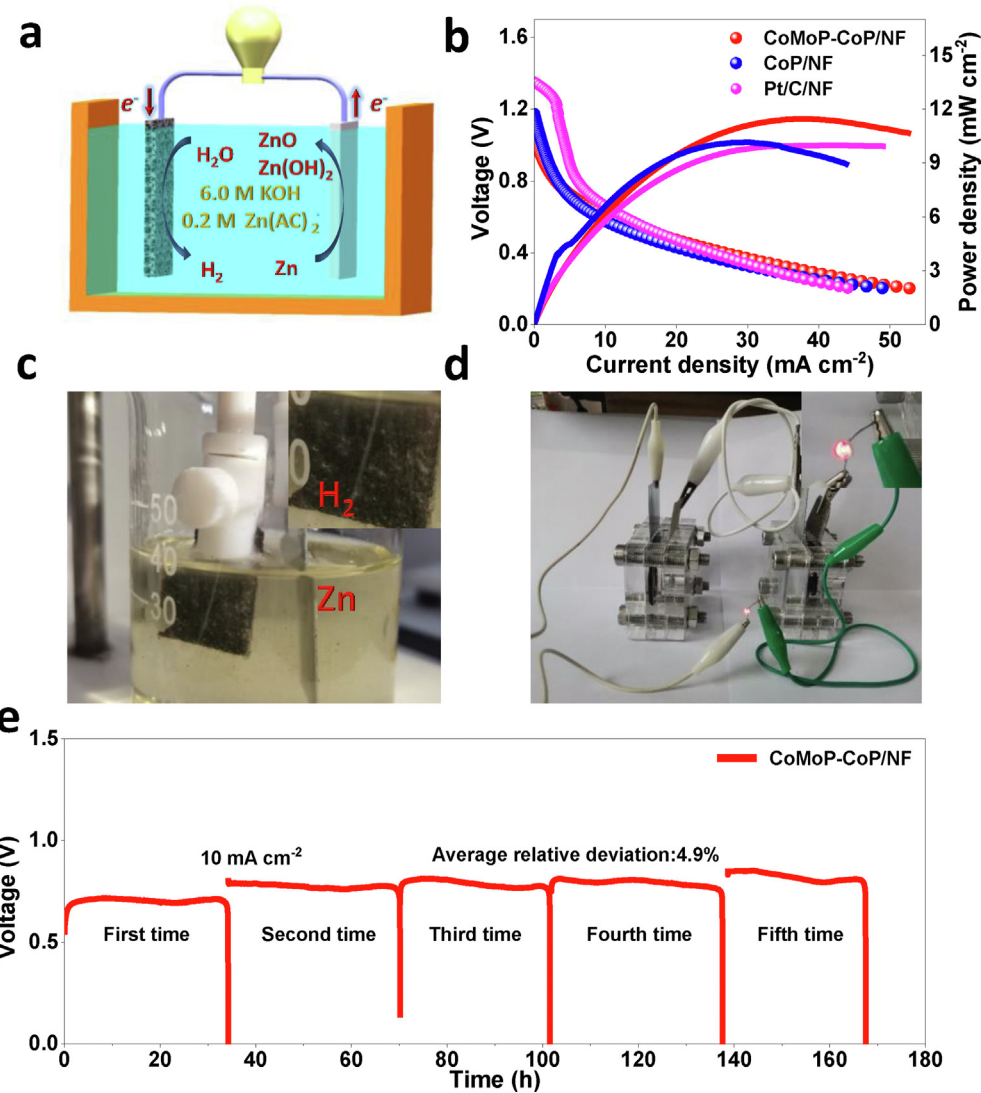


Fig. 6 – (a) The polarization curve of CoMoO<sub>4</sub>–Co(OH)<sub>2</sub>/NF<sup>(+)</sup>||CoMoP–CoP/NF<sup>(−)</sup> in 30 wt% KOH. (b) Durability tests of CoMoO<sub>4</sub>–Co(OH)<sub>2</sub>/NF<sup>(+)</sup>||CoMoP–CoP/NF<sup>(−)</sup> (30 wt% and 1.0 M KOH).



**Fig. 7 – (a)** Schematic diagram of the  $\text{Zn}-\text{H}_2\text{O}$  cell. **(b)** Polarization and power density curves about  $\text{CoMoP}-\text{CoP}/\text{NF}$ ,  $\text{CoP}/\text{NF}$  and  $\text{Pt/C}$ . **(c)** Hydrogen bubbles produced on the cathode surface of  $\text{CoMoP}-\text{CoP}/\text{NF}$ . **(d)** Picture of one red LED light lit by two  $\text{Zn}-\text{H}_2\text{O}$  cell of  $\text{CoMoP}-\text{CoP}/\text{NF}$ . **(e)** Discharge curves of  $\text{CoMoP}-\text{CoP}/\text{NF}$ . The electrolyte in Fig. 7a–e is  $6.0 \text{ M KOH}$  and  $0.2 \text{ M } \text{Zn}(\text{AC})_2$ .

## Conclusions

In summary, the  $\text{CoMoO}_4-\text{Co(OH)}_2/\text{NF}$  and  $\text{CoMoP}-\text{CoP}/\text{NF}$  combined catalysts for water splitting and  $\text{Zn}-\text{H}_2\text{O}$  cell have successfully prepared via a two-step approach of *in-situ* conversion and phosphorization. The experimental results fully proved their multi-functional, robust and stable catalytic activities derived from the hierarchical structure, array-like sheets, fast charge transfer and synergistic effect. The combination of two catalysts could achieve highly stable water splitting at high current density used in industrial condition, and the resurrection of  $\text{CoMoP}-\text{CoP}/\text{NF}$  realized the repeated and stable operation of the same  $\text{Zn}-\text{H}_2\text{O}$  cell. We believe that the novel multifunctional non-noble metal-based catalysts has a bright future of realizing hydrogen production with lower energy consumption.

## Declaration of competing interest

The authors declare that they have no known competing financial interests or personal relationships that could have appeared to influence the work reported in this paper.

## Acknowledgements

This work has been supported by the National Natural Science Foundation of China (no. 21965005), Natural Science Foundation of Guangxi Province (2020GXNSFBA297001, 2021GX NSFAA076001), Guangxi Key Laboratory of Information Materials (201028-Z), Project of High-Level Talents of Guangxi (F-KA18015) and Guangxi Technology Base and Talent Subject (GUIKE AD18126001, GUIKE AD20297039).

## Appendix A. Supplementary data

Supplementary data to this article can be found online at doi:[10.1016/j.ijhydene.2022.05.136](https://doi.org/10.1016/j.ijhydene.2022.05.136).

## REFERENCES

- [1] Zhou Y, Wang Z, Pan Z, Liu L, Xi J, Luo X, et al. Exceptional performance of hierarchical Ni-Fe (hydr)oxide@NiCu electrocatalysts for water splitting. *Adv Mater* 2019;31:1806769.
- [2] Liu Z, Yuan C, Teng F. Crystal facets-predominated oxygen evolution reaction activity of earth abundant CoMoO<sub>4</sub> electrocatalyst. *J Alloys Compd* 2019;781:460–6.
- [3] Li C, Zhang B, Li Y, Hao S, Cao X, Yang G, et al. Self-assembled Cu-Ni bimetal oxide 3D in-plane epitaxial structures for highly efficient oxygen evolution reaction. *Appl Catal B Environ* 2019;244:56–62.
- [4] Li D, Liu D, Zhao S, Lu S, Ma Y, Li M, et al. Tuning of metallic valence in CoMoP for promoting electrocatalytic hydrogen evolution. *Int J Hydrogen Energy* 2019;44:31072–81.
- [5] Kou Z, Zhang L, Ma Y, Liu X, Zang W, Zhang J, et al. 2D carbide nanomeshes and their assembling into 3D microflowers for efficient water splitting. *Appl Catal B Environ* 2019;243:678–85.
- [6] Prematuri R, Turjaman M, Sato T, Tawaraya K. The impact of nickel mining on soil properties and growth of two fast-growing tropical trees species. *Int J Res* 2020;2020:8837590.
- [7] Cao L-M, Lu D, Zhong D-C, Lu T-B. Prussian blue analogues and their derived nanomaterials for electrocatalytic water splitting. *Coord Chem Rev* 2020;407:213156.
- [8] Kou T, Wang S, Hauser JL, Chen M, Oliver SRJ, Ye Y, et al. Ni foam-supported Fe-doped  $\beta$ -Ni(OH)<sub>2</sub> nanosheets show ultralow overpotential for oxygen evolution reaction. *ACS Energy Lett* 2019;4:622–8.
- [9] Xun S, Xu Y, He J, Jiang D, Yang R, Li D, et al. MOF-derived cobalt oxides nanoparticles anchored on CoMoO<sub>4</sub> as a highly active electrocatalyst for oxygen evolution reaction. *J Alloys Compd* 2019;806:1097–104.
- [10] Wang Y-Q, Zhao L, Sui X-L, Gu D-M, Wang Z-B. Hierarchical CoP<sub>x</sub>/NiMoO<sub>4</sub> heterostructures on Ni foam as an efficient bifunctional electrocatalyst for overall water splitting. *Ceram Int* 2019;45:17128–36.
- [11] Anandhababu G, Huang Y, Babu DD, Wu M, Wang Y. Oriented growth of ZIF-67 to derive 2D porous CoPO<sub>x</sub> nanosheets for electrochemical-/photovoltage-driven overall water splitting. *Adv Funct Mater* 2018;28:1706120.
- [12] Hu H-S, Li Y, Shao Y-R, Li K-X, Deng G, Wang C-B, et al. NiCoP nanorod arrays as high-performance bifunctional electrocatalyst for overall water splitting at high current densities. *J Power Sources* 2021;484:229269.
- [13] Odynets IV, Strutynska NY, Li J, Han W, Zatovsky IV, Klyui NI. CoO<sub>x</sub>(OH)<sub>y</sub>/C nanocomposites in situ derived from Na<sub>4</sub>Co<sub>3</sub>(PO<sub>4</sub>)<sub>2</sub>P<sub>2</sub>O<sub>7</sub> as sustainable electrocatalysts for water splitting. *Dalton Trans* 2018;47:15703–13.
- [14] Yan P, Huang M, Wang B, Xia Wan, Qian M, Yan H, et al. Oxygen defect-rich double-layer hierarchical porous Co<sub>3</sub>O<sub>4</sub> arrays as high-efficient oxygen evolution catalyst for overall water splitting. *J Energy Chem* 2020;47:299–306.
- [15] Chen M, Wang N, Wang X, Zhou Y, Zhu L. Enhanced degradation of tetrabromobisphenol A by magnetic Fe<sub>3</sub>O<sub>4</sub>@ZIF-67 composites as a heterogeneous Fenton-like catalyst. *Chem Eng J* 2020;127539.
- [16] Lin D, Duan P, Yang W, Liu Y, Pan Q. Facile controlled synthesis of core-shell/yolk-shell/hollow ZIF-67@Co-LDH/
- SiO<sub>2</sub> via a self-template method. *Inorg Chem Front* 2020;7:1643–50.
- [17] Ghoshal S, Zaccarine S, Anderson GC, Martinez MB, Hurst KE, Pylypenko S, et al. ZIF 67 based highly active electrocatalysts as oxygen electrodes in water electrolyzer. *ACS Appl Energy Mater* 2019;2:5568–76.
- [18] Bao Y, Liu P, Zhang J, Wang L, Wang M, Mei H, et al. Construction of carbon quantum dots embed  $\alpha$ -Co/Ni(OH)<sub>2</sub> hollow nanocages with enhanced supercapacitor performance. *J Am Ceram Soc* 2020;103:4342–51.
- [19] Chuong ND, Thanh TD, Kim NH, Lee JH. Hierarchical heterostructures of ultrasmall Fe<sub>2</sub>O<sub>3</sub>-encapsulated MoS<sub>2</sub>/N-graphene as an effective catalyst for oxygen reduction reaction. *ACS Appl Mater Interfaces* 2018;10:24523–32.
- [20] Cheng X, Dou S, Qin G, Wang B, Yan P, Isimjan TT, et al. Rational design of highly selective nitrogen-doped Fe<sub>2</sub>O<sub>3</sub>-CNTs catalyst towards H<sub>2</sub>O<sub>2</sub> generation in alkaline media. *Int J Hydrogen Energy* 2020;45:6128–37.
- [21] Zha Q, Xu W, Li X, Ni Y. Chlorine-doped  $\alpha$ -Co(OH)<sub>2</sub> hollow nano-dodecahedrons prepared by a ZIF-67 self-sacrificing template route and enhanced OER catalytic activity. *Dalton Trans* 2019;48:12127–36.
- [22] Li H, Zhao X, Liu H, Chen S, Yang X, Lv C, et al. Sub-1.5 nm ultrathin CoP nanosheet aerogel: efficient electrocatalyst for hydrogen evolution reaction at all pH values. *Small* 2018;14:1802824.
- [23] Dang Y, He J, Wu T, Yu L, Kerns P, Wen L, et al. Constructing bifunctional 3D holey and ultrathin CoP nanosheets for efficient overall water splitting. *ACS Appl Mater Interfaces* 2019;11:29879–87.
- [24] Liu Z, Zhan C, Peng L, Cao Y, Chen Y, Ding S, et al. A CoMoO<sub>4</sub>-Co<sub>2</sub>Mo<sub>3</sub>O<sub>8</sub> heterostructure with valence-rich molybdenum for a high-performance hydrogen evolution reaction in alkaline solution. *J Mater Chem* 2019;7:16761–9.
- [25] Jia D, Gao H, Xing L, Chen X, Dong W, Huang X, et al. 3D self-supported porous NiO@NiMoO<sub>4</sub> core-shell nanosheets for highly efficient oxygen evolution reaction. *Inorg Chem* 2019;58:6758–64.
- [26] Jiang D, Xu Y, Yang R, Li D, Meng S, Chen M. CoP<sub>3</sub>/CoMoP heterogeneous nanosheet arrays as robust electrocatalyst for pH-universal hydrogen evolution reaction. *ACS Sustainable Chem Eng* 2019;7:9309–17.
- [27] Liu B, Li H, Cao B, Jiang J, Gao R, Zhang J. Few layered N, P dual-doped carbon-encapsulated ultrafine MoP nanocrystal/MoP cluster hybrids on carbon cloth: an ultrahigh active and durable 3D self-supported integrated electrode for hydrogen evolution reaction in a wide pH range. *Adv Funct Mater* 2018;28:1801527.
- [28] Gan Q, Cheng X, Chen J, Wang D, Wang B, Tian J, et al. Temperature effect on crystallinity and chemical states of nickel hydroxide as alternative superior catalyst for urea electrooxidation. *Electrochim Acta* 2019;301:47–54.
- [29] Tao K, Dan H, Hai Y, Liu L, Gong Y. Controllable synthesis of MoO linkage enhanced CoP ultrathin nanosheet arrays for efficient overall water splitting. *Appl Surf Sci* 2019;493:852–61.
- [30] Xu Y, Xie L, Li D, Yang R, Jiang D, Chen M. Engineering Ni(OH)<sub>2</sub> nanosheet on CoMoO<sub>4</sub> nanoplate Array as efficient electrocatalyst for oxygen evolution reaction. *ACS Sustainable Chem Eng* 2018;6:16086–95.
- [31] Yu H, Qi L, Hu Y, Qu Y, Yan P, Isimjan TT, et al. Nanowire-structured FeP-CoP arrays as highly active and stable bifunctional electrocatalyst synergistically promoting high-current overall water splitting. *J Colloid Interface Sci* 2021;600:811–9.
- [32] Thangavel P, Kim G, Kim KS. Electrochemical integration of amorphous NiFe (oxy)hydroxides on surface-activated carbon fibers for high-efficiency oxygen evolution in alkaline

- anion exchange membrane water electrolysis. *J Mater Chem* 2021;9:14043–51.
- [33] Harzandi AM, Shadman S, Nissimagoudar AS, Kim DY, Lim H-D, Lee JH, et al. Ruthenium core–shell engineering with nickel single atoms for selective oxygen evolution via nondestructive mechanism. *Adv Energy Mater* 2021;11:2003448.
- [34] Thangavel P, Ha M, Kumaraguru S, Meena A, Singh AN, Harzandi AM, et al. Graphene-nanoplatelets-supported NiFe-MOF: high-efficiency and ultra-stable oxygen electrodes for sustained alkaline anion exchange membrane water electrolysis. *Energy Environ Sci* 2020;13:3447–58.
- [35] Lyu F, Bai Y, Li Z, Xu W, Wang Q, Mao J, et al. Self-templated fabrication of CoO-MoO<sub>2</sub> nanocages for enhanced oxygen evolution. *Adv Funct Mater* 2017;27:1702324.
- [36] Zhang S, She G, Li S, Qu F, Mu L, Shi W. Enhancing the electrocatalytic activity of NiMoO<sub>4</sub> through a post-phosphorization process for oxygen evolution reaction. *Catal Commun* 2019;129:105725.
- [37] An L, Feng J, Zhang Y, Wang R, Liu H, Wang G-C, et al. Epitaxial heterogeneous interfaces on N-NiMoO<sub>4</sub>/NiS<sub>2</sub> nanowires/nanosheets to boost hydrogen and oxygen production for overall water splitting. *Adv Funct Mater* 2019;29:1805298.
- [38] Dou Y, Zhang L, Xu J, He C-T, Xu X, Sun Z, et al. Manipulating the architecture of atomically thin transition metal (hydr) oxides for enhanced oxygen evolution catalysis. *ACS Nano* 2018;12:1878–86.
- [39] Wang H, Li Y, Wang R, He B, Gong Y. Metal-organic-framework template-derived hierarchical porous CoP arrays for energy-saving overall water splitting. *Electrochim Acta* 2018;284:504–12.
- [40] Han X, Yu C, Huang H, Guo W, Zhao C, Huang H, et al. Phase controllable synthesis of Ni<sup>2+</sup> post-modified CoP nanowire for enhanced oxygen evolution. *Nano Energy* 2019;62:136–43.
- [41] Du X, Che P, Wang Y, Yuan C, Zhang X, Ni<sub>3</sub>S<sub>2</sub>@Co(OH)<sub>2</sub> heterostructures grown on Ni foam as an efficient electrocatalyst for water oxidation. *Int J Hydrogen Energy* 2019;44:22955–61.
- [42] Li Y, Wang C, Cui M, Chen S, Ma T. A novel strategy to synthesize CoMoO<sub>4</sub> nanotube as highly efficient oxygen evolution reaction electrocatalyst. *Catal Commun* 2019;131:105800.
- [43] Jin YZ, Li Z, Wang JQ, Li R, Li ZQ, Liu H, et al. Tuning spin state of rock-salt-based oxides by manipulation of crystallinity for efficient oxygen electrocatalysis. *Adv Energy Mater* 2018;8:1703469.
- [44] Wang F, Zhao J, Tian W, Hu Z, Lv X, Zhang H, et al. Morphology-controlled synthesis of CoMoO<sub>4</sub> nanoarchitectures anchored on carbon cloth for high-efficiency oxygen oxidation reaction. *RSC Adv* 2019;9:1562–9.
- [45] Wang X, Rong F, Huang F, He P, Yang Y, Tang J, et al. Facile synthesis of hierarchical CoMoO<sub>4</sub>@Ni(OH)<sub>2</sub> core-shell nanotubes for bifunctional supercapacitors and oxygen electrocatalysts. *J Alloys Compd* 2019;789:684–92.
- [46] Wang P, Liu X, Yan Y, Cao J, Feng J, Qi J. Exploring CoP core-shell nanosheets by Fe and Zn dual cation doping as efficient electrocatalysts for overall water splitting. *Catal Sci Technol* 2020;10:1395–400.
- [47] Feng Y, Xu C, Hu E, Xia B, Ning J, Zheng C, et al. Construction of hierarchical FeP/Ni<sub>2</sub>P hollow nanospindles for efficient oxygen evolution. *J Mater Chem* 2018;6:14103–11.
- [48] Yang F, Chen X, Li Z, Wang D, Liu L, Ye J. Ultrathin FeP nanosheets as an efficient catalyst for electrocatalytic water oxidation: promoted intermediates adsorption by surface defects. *ACS Appl Energy Mater* 2020;3:3577–85.
- [49] Zhong J, Wu T, Wu Q, Du S, Chen D, Chen B, et al. N- and S-co-doped graphene sheet-encapsulated Co<sub>9</sub>S<sub>8</sub> nanomaterials as excellent electrocatalysts for the oxygen evolution reaction. *J Power Sources* 2019;417:90–8.
- [50] Wang M, Fu W, Du L, Wei Y, Rao P, Wei L, et al. Surface engineering by doping manganese into cobalt phosphide towards highly efficient bifunctional HER and OER electrocatalysis. *Appl Surf Sci* 2020;515:146059.
- [51] Li Y, Jiang Z, Huang J, Zhang X, Chen J. Template-synthesis and electrochemical properties of urchin-like NiCoP electrocatalyst for hydrogen evolution reaction. *Electrochim Acta* 2017;249:301–7.
- [52] Ma Y-Y, Wu C-X, Feng X-J, Tan H-Q, Yan L-K, Liu Y, et al. Highly efficient hydrogen evolution from seawater by a low-cost and stable CoMoP@C electrocatalyst superior to Pt/C. *Energy Environ Sci* 2017;10:788–98.
- [53] Meng C, Lin M, Sun X, Chen X, Chen X, Du X, et al. Laser synthesis of oxygen vacancy-modified CoOOH for highly efficient oxygen evolution. *ChemComm* 2019;55:2904–7.
- [54] Chi K, Tian X, Wang Q, Zhang Z, Zhang X, Zhang Y, et al. Oxygen vacancies engineered CoMoO<sub>4</sub> nanosheet arrays as efficient bifunctional electrocatalysts for overall water splitting. *J Catal* 2020;381:44–52.
- [55] Wang L, Huang Z, Huang H, Zhong S, Huang M, Isimjan TT, et al. Electron-transfer enhanced sponge-like CrP-Re<sub>2</sub>P as a robust bifunctional electrocatalyst for high-current overall water splitting and Zn–H<sub>2</sub>O cell. *Electrochim Acta* 2022;404:139598.
- [56] Liu Y-C, Koza JA, Switzer JA. Conversion of electrodeposited Co(OH)<sub>2</sub> to CoOOH and Co<sub>3</sub>O<sub>4</sub>, and comparison of their catalytic activity for the oxygen evolution reaction. *Electrochim Acta* 2014;140:359–65.
- [57] Zhou H, Yu F, Zhu Q, Sun J, Qin F, Yu L, et al. Water splitting by electrolysis at high current densities under 1.6 volts. *Energy Environ Sci* 2018;11:2858–64.
- [58] Wang B, Huang H, Sun T, Yan P, Isimjan TT, Tian J, et al. Dissolution reconstruction of electron-transfer enhanced hierarchical NiS<sub>x</sub>-MoO<sub>2</sub> nanosplices as a promising industrialized hydrogen evolution catalyst beyond Pt/C. *J Colloid Interface Sci* 2020;567:339–46.